

# First-principles calculation of the lattice thermal conductivities of $\alpha$ -, $\beta$ -, and $\gamma$ - $\text{Si}_3\text{N}_4$

Kazuyoshi Tatsumi,<sup>1,2,\*</sup> Atsushi Togo,<sup>2</sup> and Isao Tanaka<sup>2,3,4</sup>

<sup>1</sup>Advanced Measurement Technology Center, Institute of Materials and Systems for Sustainability, Nagoya University, Chikusa, Nagoya 464-8603, Japan

<sup>2</sup>Center for Elements Strategy Initiative for Structural Materials, Kyoto University, Sakyo, Kyoto 606-8501, Japan

<sup>3</sup>Department of Materials Science and Engineering, Kyoto University, Sakyo, Kyoto 606-8501, Japan

<sup>4</sup>Nanostructures Research Laboratory, Japan Fine Ceramics Center, Atsuta, Nagoya 456-8587, Japan

Lattice thermal conductivities of  $\alpha$ -,  $\beta$ - and  $\gamma$ - $\text{Si}_3\text{N}_4$  single crystals are investigated from *ab-initio* anharmonic lattice dynamics, within the single-mode relaxation-time approximation of the linearized phonon Boltzmann transport equation. At 300 K, the lattice thermal conductivity of  $\beta$ - $\text{Si}_3\text{N}_4$  is calculated as  $\kappa_{xx} = 73$  and  $\kappa_{zz} = 198$  (in units of  $\text{Wm}^{-1}\text{K}^{-1}$ ), that is consistent with the reported experimental values of 69 and 180, respectively. For  $\alpha$ - $\text{Si}_3\text{N}_4$ ,  $\kappa_{xx} = 69$  and  $\kappa_{zz} = 99$  are obtained. The difference of anisotropy between  $\alpha$ - $\text{Si}_3\text{N}_4$  and  $\beta$ - $\text{Si}_3\text{N}_4$  is originated from their characteristic difference in the phonon band structures, although their crystal structures are similar in their local atomic coordinates. In  $\alpha$ - $\text{Si}_3\text{N}_4$ , acoustic-mode phonons below 6 THz are the main heat carriers. In  $\beta$ - $\text{Si}_3\text{N}_4$ , the phonon modes up to 12 THz contribute to the lattice thermal conductivity. In  $\gamma$ - $\text{Si}_3\text{N}_4$ ,  $\kappa = 81$  is obtained. The distribution of phonon mode contributions to lattice thermal conductivity with respect to phonon frequency is found to closely resemble  $\kappa_{xx}$  of  $\beta$ - $\text{Si}_3\text{N}_4$  although the phonon lifetimes of  $\gamma$ - $\text{Si}_3\text{N}_4$  are twice shorter than those of  $\beta$ - $\text{Si}_3\text{N}_4$ .

## I. INTRODUCTION

Several nitride insulators are known to exhibit high thermal conductivities and are important for heat transfer materials at elevated temperatures. For example, Slack *et al.*<sup>1</sup> reported that wurtzite-type w-AlN has thermal conductivity of  $\gg 100 \text{ Wm}^{-1}\text{K}^{-1}$ .  $\text{Si}_3\text{N}_4$  has become another promising thermal conductive insulator as its thermal conductivity has been improved up to  $177 \text{ Wm}^{-1}\text{K}^{-1}$  through advances in ceramic technologies related to the densification and microstructure control.<sup>2-5</sup> Since the  $\text{Si}_3\text{N}_4$  ceramics also exhibit high mechanical strength at elevated temperatures, they are regarded as ideal materials for the use in various applications, such as engine components, gas turbines, and heat sink substrates of power semiconductor devices.

At atmospheric pressure,  $\text{Si}_3\text{N}_4$  exists in one of two phases,  $\alpha$  and  $\beta$ , which are generally considered as low- and high-temperature phases, respectively.<sup>2,5,6</sup> Their crystal structures belong to the space groups of  $P31c$ <sup>7</sup> and  $P6_3/m$ <sup>8</sup>, respectively. These structures are formed by different stacking of equivalent basal layer structures originated by  $\text{SiN}_4$  tetrahedra.<sup>9</sup> In Fig. 1 these layer structures are depicted from the principal direction, as A, B, C, and D in the  $\alpha$  phase and A and B in the  $\beta$  phase. The stacking manners in  $\alpha$  and  $\beta$ - $\text{Si}_3\text{N}_4$  are thus as ABCDABCD.. and ABAB.., respectively. The  $\alpha$  phase has additional two layer structures of C and D, which are related to the A and B by the  $c$  glide operation.<sup>9</sup> Along this direction the lattice constant of the  $\alpha$  phase is approximately two times longer than that of the  $\beta$  phase.

Li *et al.*<sup>11</sup> reported using high-resolution thermoreflectance microscopy that the thermal conductivity of a rod-shaped  $\beta$ - $\text{Si}_3\text{N}_4$  grain in a ceramic was 69 and 180

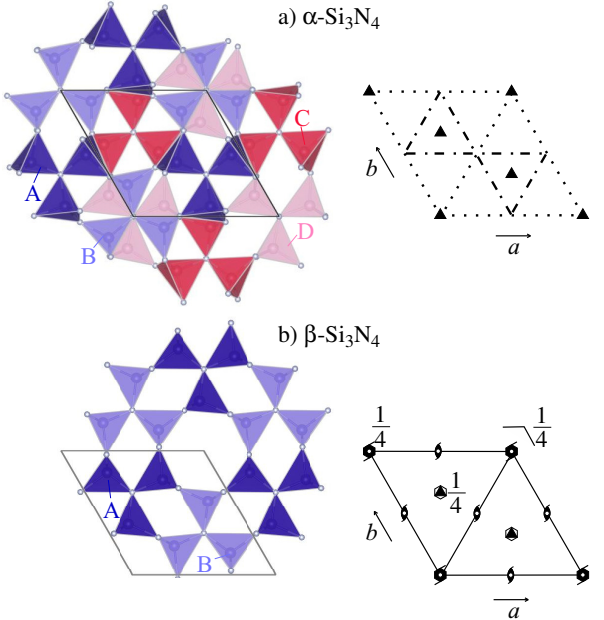


FIG. 1. (color online) Crystal structures of  $\alpha$ - and  $\beta$ - $\text{Si}_3\text{N}_4$ . Stacking of  $\text{SiN}_4$  tetrahedron layers are shown in left. (a) ABCDABCD.. for  $\alpha$ - $\text{Si}_3\text{N}_4$ . (b) ABAB.. for  $\beta$ - $\text{Si}_3\text{N}_4$ . Space group diagrams<sup>10</sup> in  $P31c$  ( $\alpha$ - $\text{Si}_3\text{N}_4$ ) and  $P6_3/m$  ( $\beta$ - $\text{Si}_3\text{N}_4$ ) are shown in right.

$\text{Wm}^{-1}\text{K}^{-1}$  along the  $a$  and  $c$  axes, respectively. We consider the anisotropy of  $\kappa_{zz}/\kappa_{xx} \sim 3$  is relatively large. Several techniques have been reported to align  $c$ -axis directions of  $\beta$ - $\text{Si}_3\text{N}_4$  grains in a ceramic.<sup>12-15</sup> The thermal conductivity of the textured ceramics would match or exceed that of w-AlN.

Although the fabrication of millimeter-sized  $\beta$ - $\text{Si}_3\text{N}_4$

single crystals has been reported,<sup>16</sup> the thermal conductivity of a single crystal of any  $\text{Si}_3\text{N}_4$  phase has not yet been experimentally determined. Watari<sup>17</sup> discussed that the anisotropy in the thermal conductivity of  $\beta\text{-Si}_3\text{N}_4$  phase grains may not stem from the intrinsic crystal properties, but rather, from the selective removal of crystal defects along the  $c$  axis of the grains. Theoretically, Hirosaki *et al.*<sup>18</sup> estimated the room-temperature lattice thermal conductivities (LTCs) by applying the Green-Kubo formulation to the molecular dynamics (MD) method with the interatomic potentials proposed by Vashishta *et al.*<sup>19</sup>. They calculated  $\kappa_{xx}$  and  $\kappa_{zz}$  of  $\alpha\text{-Si}_3\text{N}_4$  as 105 and 225  $\text{Wm}^{-1}\text{K}^{-1}$ , and those of  $\beta\text{-Si}_3\text{N}_4$  as 170 and 450  $\text{Wm}^{-1}\text{K}^{-1}$ , respectively. Although the absolute values were more than two times larger, the ratio  $\kappa_{zz}/\kappa_{xx}$  agreed well with the experimental results obtained by Li *et al.*<sup>11</sup> Moreover, the MD results suggest that the different stacking orders between  $\alpha$ - and  $\beta\text{-Si}_3\text{N}_4$  alter their LTC largely. On the other hand, the recent LTC calculation based on first principles calculation and Boltzmann transport theory has shown that in many polymorphs of the wurtzite and zincblende structures, which have different stacking orders of the densest atom planes as ABAB.. and ABCABC.., these orders merely alter the LTCs.<sup>20</sup> It is interesting to investigate it using this approach for  $\alpha$ - and  $\beta\text{-Si}_3\text{N}_4$ .

In addition to these phases, a cubic spinel phase ( $\gamma\text{-Si}_3\text{N}_4$ ) can be formed upon compression and in-situ heating.<sup>21,22</sup> The reported transition pressures were scattered from 10 to 36 GPa depending on the experimental conditions.<sup>23</sup> The produced  $\gamma$  phase can be experimentally quenched to atmospheric pressure and room temperature. Its thermal conductivity has not been experimentally reported; it has been estimated only by the Slack model.<sup>24</sup> **We apply the same first principles approach to this phase, for systematic understanding of the LTC in the  $\text{Si}_3\text{N}_4$  system.**

The present study aims to qualitatively understand the LTC tensors among the three  $\text{Si}_3\text{N}_4$  phases by means of the first principles approach. After the methodology section, we examine the validity of the present LTC results first. Then we investigate the characteristics in the LTCs in detail.

## II. COMPUTATIONAL PROCEDURES

### A. Lattice thermal conductivity calculation

The LTCs were calculated by solving the linearized Boltzmann transport equation (LBTE) within the single-mode relaxation time approximation (single-mode RTA). We also tried the direct-solution of LBTE<sup>25</sup> and leave its calculated LTC values in the following section. The difference of LTCs between by the single-mode RTA and by the direct solution was found minor for our discussion. Therefore we limited our research to use the single-mode RTA to take advantage of its intuitive closed form of

LTCs.

In the following sections, we denote a phonon mode by  $\lambda = (\mathbf{q}, p)$  with the set of the phonon wave vector  $\mathbf{q}$  and band index  $p$  and  $-\lambda \equiv (-\mathbf{q}, p)$ . The relaxation time due to phonon-phonon scattering was obtained as reciprocal of linewidth,  $\tau_{\lambda,\text{ph-ph}} = (2\Gamma_{\lambda})^{-1}$ , where the linewidth that we employed in this study is as follows:

$$\begin{aligned} \Gamma_{\lambda} = & \frac{18\pi}{\hbar^2} \sum_{\lambda'\lambda''} |\Phi_{-\lambda\lambda'\lambda''}|^2 \times \\ & \{(n_{\lambda'} + n_{\lambda''} + 1)\delta(\omega_{\lambda} - \omega_{\lambda'} - \omega_{\lambda''}) + \\ & (n_{\lambda'} - n_{\lambda''})[\delta(\omega_{\lambda} + \omega_{\lambda'} - \omega_{\lambda''}) - \delta(\omega_{\lambda} - \omega_{\lambda'} + \omega_{\lambda''})]\}. \end{aligned} \quad (1)$$

Here  $\omega_{\lambda}$  is the harmonic phonon frequency of the phonon mode  $\lambda$ ,  $n_{\lambda} = [\exp(\hbar\omega_{\lambda}/k_{\text{B}}T) - 1]^{-1}$  is the Bose-Einstein distribution at temperature  $T$ , and  $\Phi_{\lambda\lambda'\lambda''}$  denotes the three-phonon-scattering strength.  $\Phi_{\lambda\lambda'\lambda''}$  was obtained by usual coordinate transformation of third-order IFCs from direct space to phonon space.<sup>20</sup> The second- and third-order real-space IFCs were obtained from the *ab initio* calculation, whose details are written in the next section.

In order to compare the more realistic results of the calculated LTC with the experimental data, the isotopic scattering effect due to the natural isotope distribution was taken into account according to the second-order perturbation theory.<sup>26</sup> With the relaxation times of the phonon-phonon scattering and isotopic scattering,  $\tau_{\lambda,\text{ph-ph}}$  and  $\tau_{\lambda,\text{iso}}$ , the total relaxation time for a phonon mode was assumed to be  $1/\tau_{\lambda} = 1/\tau_{\lambda,\text{ph-ph}} + 1/\tau_{\lambda,\text{iso}}$ , according to Matthiessen's rule.

These LTCs were calculated with the phonon-phonon interaction calculation code PHONO3PY,<sup>20</sup> while the harmonic phonon states were analyzed with the phonon calculation code PHONOPY.<sup>27</sup>

The available experimental thermal conductivity data of the  $\text{Si}_3\text{N}_4$  system have been measured on the polycrystalline samples and not measured from any single crystals. In order to consider the effect of various lattice defects in the polycrystalline samples, such as grain boundaries, impurities, and vacancies, we crudely took them into account by a relaxation time  $\tau_{\lambda,\text{bs}} = L/|\mathbf{v}_{\lambda}|$  of a phonon boundary scattering model, where  $\mathbf{v}_{\lambda} = \nabla_{\mathbf{q}}\omega_{\lambda}$  is the group velocity and  $L$  a parameter regarding to the boundary mean free path. We consider  $\tau_{\lambda,\text{bs}}$  as a variable parameter and included it to LTCs according to Matthiessen's rule.

The closed form of the LTC tensors within RTA were obtained via

$$\boldsymbol{\kappa}(T) = \frac{1}{N_{\mathbf{q}}\Omega} \sum_{\lambda} \tau_{\lambda}(T) \mathbf{v}_{\lambda} \otimes \mathbf{v}_{\lambda} c_{\lambda}(T), \quad (2)$$

where  $N_{\mathbf{q}}$  is the number of  $\mathbf{q}$ -points,  $\Omega$  is the unit cell volume, and  $c_{\lambda}$  is the mode heat capacity. To analyze the LTC in detail, we calculate the cumulative thermal

conductivity:

$$\kappa^c(\omega) = \frac{1}{N_{\mathbf{q}}\Omega} \int_0^\omega \sum_\lambda \tau_\lambda(T) \mathbf{v}_\lambda \otimes \mathbf{v}_\lambda c_\lambda(T) \delta(\omega' - \omega) d\omega', \quad (3)$$

and its derivative  $\frac{\partial \kappa^c(\omega)}{\partial \omega}$  to see the phonon mode contributions to the LTC.

### B. Computational details

The IFCs were calculated using the first-principles projector augmented wave method<sup>28</sup> (VASP code<sup>29–31</sup>). The generalized gradient approximation (GGA) parameterized by Perdew, Burke, and Ernzerhof<sup>32</sup> was used for the exchange correlation potential. A plane wave energy cut-off of 500 eV was employed. The crystal structures were optimized until the convergence in the residual forces acting on the constituent atoms was less than  $10^{-6}$  eV/Å. The structural optimization was firstly performed for a temperature of 0 K and 0 GPa. Here the temperature and pressure were considered only for the electronic system and the zero point lattice vibration was not taken into account. The calculated lattice parameters were  $a = 7.808$  Å and  $c = 5.659$  Å for the  $\alpha$  phase,  $a = 7.660$  Å and  $c = 2.925$  Å for the  $\beta$  phase, and  $a = 7.787$  Å for the  $\gamma$  phase, which agree with the experimental data<sup>7,8,33</sup> within +0.7 % errors. The lattice volume optimized at 0 K and 0 GPa within the local density approximation (LDA)<sup>34</sup> for the exchange correlation potential was, for  $\beta$ -Si<sub>3</sub>N<sub>4</sub>, 3 % smaller than the volume with GGA, which is a typical volume contraction of LDA. In our test using  $\beta$ -Si<sub>3</sub>N<sub>4</sub> at 0 K and 0 GPa, the LTC calculated with LDA was larger by 2.6 % than that with GGA. For our discussion, this difference is enough small, therefore the impact of choice of exchange correlation potential is considered to be minor in our study.

Supercell and finite difference approaches were used to calculate the IFCs.<sup>35</sup> The  $1 \times 1 \times 2$ ,  $1 \times 1 \times 3$ , and  $1 \times 1 \times 1$  supercells of the conventional unit cells were adopted for the third-order IFCs of the  $\alpha$ ,  $\beta$ , and  $\gamma$  phases, respectively, while the larger supercells  $3 \times 3 \times 4$ ,  $3 \times 3 \times 8$  and  $2 \times 2 \times 2$  were adopted for the respective second-order IFCs. The constant atomic displacement distance was set to 0.03 Å. Table I shows the calculated LTC values for several different choices of supercell sizes, indicating that our calculated LTCs are reasonably converging with respect to the supercell sizes.

Non-analytical term correction<sup>36</sup> was applied to the second-order IFC to take into account the long range Coulomb forces present in ionic crystals. For the correction, Born effective charges were calculated by using the density functional perturbation theory (DFPT). Ref!

Uniform  $\mathbf{k}$ -point sampling meshes of  $4 \times 4 \times 2$ ,  $4 \times 4 \times 3$ , and  $3 \times 3 \times 3$  were used for the third-order IFCs of the  $\alpha$ ,  $\beta$ , and  $\gamma$  phases. For the former two phases the center of the  $a^*-b^*$  plane were sampled though the off-center

TABLE I. Calculated lattice thermal conductivities (LTC) of  $\alpha$ -,  $\beta$ -, and  $\gamma$ -Si<sub>3</sub>N<sub>4</sub> (WK<sup>-1</sup>m<sup>-1</sup>) at 300 K with respect to several combinations of supercell sizes.

Phase	Supercell (# of atoms)		LTC	
	3 <sup>rd</sup> FC	2 <sup>nd</sup> FC	<i>xx</i>	<i>zz</i>
$\alpha$	1 $\times$ 1 $\times$ 1 (28)	1 $\times$ 1 $\times$ 1 (28)	37	57
	1 $\times$ 1 $\times$ 2 (56)	1 $\times$ 1 $\times$ 2 (56)	41	79
	1 $\times$ 1 $\times$ 1 (28)	2 $\times$ 2 $\times$ 2 (224)	55	81
	1 $\times$ 1 $\times$ 2 (56)	2 $\times$ 2 $\times$ 2 (224)	67	95
	1 $\times$ 1 $\times$ 2 (56)	2 $\times$ 2 $\times$ 3 (336)	68	97
	1 $\times$ 1 $\times$ 2 (56)	3 $\times$ 3 $\times$ 4 (1008)	68	100
$\beta$	1 $\times$ 1 $\times$ 2 (28)	1 $\times$ 1 $\times$ 2 (28)	44	173
	1 $\times$ 1 $\times$ 2 (28)	2 $\times$ 2 $\times$ 4 (224)	76	208
	1 $\times$ 1 $\times$ 3 (42)	2 $\times$ 2 $\times$ 4 (224)	71	194
	1 $\times$ 1 $\times$ 3 (42)	2 $\times$ 2 $\times$ 5 (280)	72	196
	1 $\times$ 1 $\times$ 3 (42)	3 $\times$ 3 $\times$ 8 (1008)	73	199
$\gamma$	1 $\times$ 1 $\times$ 1 (56)	1 $\times$ 1 $\times$ 1 (56)	72	
	1 $\times$ 1 $\times$ 1 (56)	2 $\times$ 2 $\times$ 2 (448)	77	
	1 $\times$ 1 $\times$ 1 (56)	3 $\times$ 3 $\times$ 3 (56)	79	

grids along  $c^*$ -axis were sampled. For the  $\gamma$  phase, non- $\Gamma$  center mesh was used. For the second-order IFC, the  $\Gamma$ -point was only sampled for the  $\alpha$  and  $\beta$  phase supercells and the only one  $\mathbf{k} = (0.5, 0.5, 0.5)$  point was sampled for the  $\gamma$  phase supercell. The  $\mathbf{q}$ -point sampling meshes of  $10 \times 10 \times 14$ ,  $10 \times 10 \times 26$ , and  $12 \times 12 \times 12$  were used to calculate the LTCs in Eq. (2) for the  $\alpha$ ,  $\beta$ , and  $\gamma$  phases.

We examined the effect of thermal expansion on the theoretical LTC values as follows: For  $\beta$ -Si<sub>3</sub>N<sub>4</sub>, the equilibrium lattice volumes at 300, 600, 900, 1200 and 1500 K were obtained within the quasi-harmonic approximation (QHA)<sup>37</sup>. With the equilibrium lattice volumes, LTC values for the temperatures were calculated and compared with those calculated with the lattice volume optimized at 0 K. The differences were found less than 1 %. The degree of the differences is similar to the case of Si and Ge<sup>38</sup>. For the present study, this effect is negligible and the LTC values calculated with the lattice volume optimized at 0 K are represented.

We calculated volumetric thermal expansion coefficients and compared them with the reported experimental values so as to check the validity of the present calculation, because the thermal expansion is originated from the anharmonicity of the interatomic potential as well as lattice thermal conduction. The calculated values are  $4.31 \times 10^{-6}$  and  $4.19 \times 10^{-6}$  K<sup>-1</sup> at 300 K for the  $\alpha$  and  $\beta$  phases, while the experimental values were 3.75 and 3.55 ( $10^{-6}$  K<sup>-1</sup>)<sup>39</sup>. The present calculation reproduced the experimental tendency where the  $\alpha$  phase has a slightly larger thermal expansion coefficient than the  $\beta$  phase, supporting that the present calculations enable us to qualitatively compare the LTC values of the Si<sub>3</sub>N<sub>4</sub> phases.

In order to compare the microscopic phonon properties

among the three phases at the same conditions, those results calculated at 0 GPa are shown and discussed. For the  $\gamma$  phase, this means that we assume the condition of virtually quenched  $\gamma$  phase at 0 GPa from the high pressure. To examine the analytical continuity of the properties with respect to pressures, we calculated LTC of  $\gamma$  phase at 10, 20, and 40 GPa as shown in Fig. 8, where the phenomenological behaviour of linear dependence of LTC with respect to pressure with the calculated slope of  $2.89 \text{ Wm}^{-1}\text{K}^{-1}\text{GPa}^{-1}$  was reproduced as similar to Ref. 40. By this, we consider that the microscopic values are also varied smoothly with the pressure and those at 0 GPa are valuable to compare with the  $\alpha$  and  $\beta$  phases.

### C. Direct solution of LBTE

The merit to employ the single-mode RTA for thermal conductivity calculation is the closed form, by which we can intuitively understand the qualitative character of LTC in terms of the relaxation time and group velocity. The microscopic understanding of the full solution of LBTE is still under the development<sup>41</sup> and the microscopic picture based on collective phonons<sup>42</sup> will require more complicated investigation although it is known that the single-mode RTA solution of LBTE often underestimates the full solution.<sup>38,43</sup>

For the  $\alpha$  and  $\beta$  phases, we adopted a direct solution of LBTE<sup>25</sup>, which is one of the methods of LBTE full solutions. The LTC values of the direct solution without the isotope effect were  $69$  and  $102 \text{ Wm}^{-1}\text{K}^{-1}$  for  $\kappa_{xx}$  and  $\kappa_{zz}$  of the  $\alpha$  phase and  $76$  and  $238 \text{ Wm}^{-1}\text{K}^{-1}$  for those of the  $\beta$  phase, respectively, while the corresponding single-mode RTA values were  $70$  and  $102 \text{ Wm}^{-1}\text{K}^{-1}$  for the  $\alpha$  phase and  $76$  and  $210 \text{ Wm}^{-1}\text{K}^{-1}$  for the  $\beta$  phase. The  $\kappa_{zz}$  of the direct solution in the  $\beta$  phase was 13 % larger than that of the single-mode RTA solution. Since the LTC difference between the LBTE solutions is not significant, we expect the physics on LTC is well understood within RTA in the current level of our interest. Therefore, the present study discusses the physics using the results of RTA.

## III. RESULTS AND DISCUSSION

### A. Lattice thermal conductivities

In Table II, the theoretical LTC values at 300 K are compared with the previously reported experimental<sup>5,11,44</sup> and theoretical<sup>18,20,24</sup> values. The present calculation results agree better with the experimental  $\kappa_{xx}$  and  $\kappa_{zz}$  of  $\beta\text{-Si}_3\text{N}_4$ , compared with the references of the Slack model<sup>24</sup> and MD<sup>18</sup> results. The directional averages of the present  $\kappa_{ii}$  in the  $\alpha$ ,  $\beta$ , and  $\gamma$  phases are 79, 115, and  $81 \text{ Wm}^{-1}\text{K}^{-1}$ . The value of the  $\gamma$  phase is similar to that of the  $\alpha$  phase, in spite of comparatively large

TABLE II. Calculated thermal conductivities of  $\alpha\text{-Si}_3\text{N}_4$  (trigonal),  $\beta\text{-Si}_3\text{N}_4$  (trigonal), and  $\gamma\text{-Si}_3\text{N}_4$  (cubic) at 300 K, compared with the experimental data. Theoretical bulk modulus  $B$  in units of GPa, calculated by the authors by using the present band method, are presented in the fourth column.

	This work			Ref. Theo.			Ref. Expt.		
	$\kappa_{xx}$	$\kappa_{zz}$	$B$	$\kappa$	$\kappa_{xx}$	$\kappa_{zz}$	$\kappa$	$\kappa_{xx}$	$\kappa_{zz}$
$\alpha\text{-Si}_3\text{N}_4$	68	100	224	70 <sup>a</sup>	105 <sup>b</sup>	225 <sup>b</sup>	59 <sup>d</sup>	-	-
$\beta\text{-Si}_3\text{N}_4$	73	199	237	250 <sup>a</sup>	170 <sup>b</sup>	450 <sup>b</sup>	122 <sup>e</sup>	69 <sup>f</sup>	180 <sup>f</sup>
$\gamma\text{-Si}_3\text{N}_4$	77	-	296	80 <sup>a</sup>	-	-	-	-	-

<sup>a</sup> Ref. 24, Slack model.

<sup>b</sup> Ref. 18, molecular dynamics (Green-Kubo).

<sup>c</sup> Ref. 44, thin film.

<sup>d</sup> Ref. 5, poly-crystals.

<sup>e</sup> Ref. 11, single crystalline grains of poly-crystals.

difference in their bulk modulus ( $B$ ) that is also shown in Table II.

It can be seen that the theoretical LTC of  $\beta\text{-Si}_3\text{N}_4$  is markedly more anisotropic than those of the  $\alpha$  phase. The theoretical LTC of  $\beta\text{-Si}_3\text{N}_4$  is in good agreement with the corresponding experimental data for individual grains reported by Li *et al.*<sup>11</sup>, indicating that the experimentally reported large anisotropy in the thermal conductivities of  $\beta\text{-Si}_3\text{N}_4$  stems from the intrinsic properties of the crystal, rather than specific defects induced during the sample preparation process.

Fig. 2 shows the theoretical LTCs of the  $\alpha$  and  $\beta$  phases as a function of  $T$ , in comparison with the reference experimental data<sup>5,11,44</sup>, which were measured with the polycrystalline samples. The values of the polycrystalline bulk samples are unable to directly compare with these theoretical LTC tensors because the microstructures of the bulk samples largely affect the thermal conductivities: The thermal conductivity can be decreased due to the phonon scattering at lattice defects in the polycrystalline sample. Moreover, the thermal conductivity can be deviated from  $\sum_i \kappa_{ii}/3$ , a simple directional average of  $\kappa_{ii}$ , because inequivalent weights can be supposed on the  $\kappa_{ii}$  terms according to the shapes of the constituent crystal grains. We represented these inequivalent weights by a parameter  $0 \leq w \leq 1$  and approximated theoretical LTC of the polycrystalline bulk sample as  $\kappa = w\kappa_{xx} + (1-w)\kappa_{zz}$ . The parameter was adjusted to result in the least square difference between the theoretical and experimental LTC values. If we adopt the simple boundary scattering model, both the parameters  $L$  and  $w$  were optimized for the least square fit.

The theoretical LTC without the simple phonon boundary scattering model is nearly inversely proportional to  $T$  because  $n_\lambda$  in Eq. (1) can be reduced to  $\exp(-\hbar\omega_\lambda/k_B T)$ . In Fig. 2-a, the temperature dependence of the experimental data of a chemically vapor-deposited  $\alpha\text{-Si}_3\text{N}_4$  sample<sup>44</sup> is deviated from inverse proportion considerably, intersecting the theoretical curves of the  $\kappa_{xx}$  and  $\kappa_{zz}$ . Thus no value of  $w$  adjusts the the-

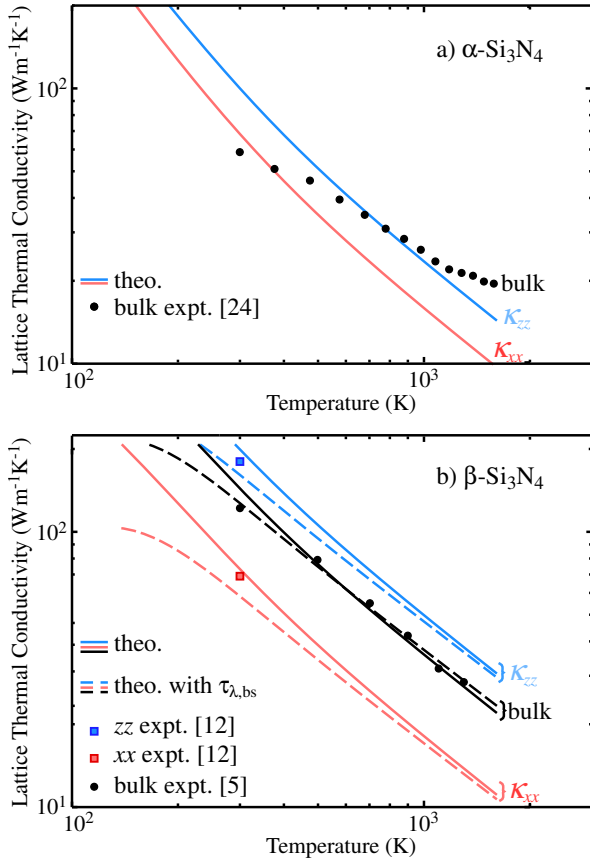


FIG. 2. (color online) Temperature dependence of LTC for  $\alpha$ - and  $\beta$ -Si<sub>3</sub>N<sub>4</sub>. For  $\beta$ -Si<sub>3</sub>N<sub>4</sub>, the LTC with the boundary scattering effect are shown by broken curves. Theoretical LTC for the bulk  $\beta$ -Si<sub>3</sub>N<sub>4</sub> sample are also shown to be compared with the experimental data of the bulk sample.

oretical LTC to the experimental curve. The full solution of LBTE would negligibly cure the disagreement. Including the simple phonon lifetime of boundary scattering,  $\tau_{\lambda,bs} = L/|\mathbf{v}_{\lambda}|$ , into the total phonon lifetime according to Matthiessen's rule, could not explain the discrepancy as well. A  $L$  value of  $0.6 \mu\text{m}$ , which was much smaller than the experimental grain size  $10 \mu\text{m}$ , decreased the room-temperature theoretical  $\kappa_{xx}$  and  $\kappa_{zz}$  values toward the experimental values, but severely underestimated the experimental values at the high temperature side. At present, the reason for the discrepancy between the theoretical and experimental behaviors is unclear. Although the crystal structure of the experimental sample was characterized as  $\alpha$ -Si<sub>3</sub>N<sub>4</sub>, significant lattice defects might exist in the as-deposited sample as pointed out by Hirosaki *et al.*<sup>18</sup> and the simple phonon boundary scattering model might fail to describe their effects. The experimental values of the  $\beta$  phase ceramic bulk<sup>5</sup> in Fig. 2-b fall well between the calculated values of  $\kappa_{xx}$  and  $\kappa_{zz}$ , being nearly parallel to the theoretical  $\kappa_{xx}$  and  $\kappa_{zz}$  curves. If we compare the experimental values with  $\sum_i \kappa_{ii}/3$ , which is a simple directional average, the

calculation shows slight underestimations with respect to the experiment, which can be understood from an experimentally tailored microstructure containing large  $\beta$ -Si<sub>3</sub>N<sub>4</sub> grains selectively grown along the  $c$  axis.<sup>5</sup>

The theoretical curve adjusted with  $w = 0.44$  explains well the experimental data of the poly-crystal bulk in Fig. 2-b. For the effects of lattice defects most of which are grain boundaries, we included  $\tau_{\lambda,bs}$  with  $L = 0.6 \mu\text{m}$  to further fit the theoretical curve ( $w = 0.33$ ) to the experimental data. The  $L$  value is slightly smaller than the average grain size ( $2 \mu\text{m}$ )<sup>5</sup> of the experimental polycrystalline sample. Fig. 2-b also contains the experimental  $\kappa_{xx}$  and  $\kappa_{zz}$  at room temperature by filled squares, which are in-between the theoretical components with and without  $\tau_{\lambda,bs}$ .

## B. Dispersion curves

Figure 3 shows the phonon band diagrams of the three Si<sub>3</sub>N<sub>4</sub> phases. The entire band diagrams are almost identical to those reported earlier<sup>23,45</sup>. However, here we focus on the group velocities on high-symmetry paths for the entire frequency range. This has not been investigated by the previous works.

The acoustic branches in the  $\alpha$  phase highlighted in red in Fig. 3-a do not increase their frequencies much more than those along the other paths,  $\Gamma$ -K or  $\Gamma$ -M. The frequency maxima along the  $\Gamma$ -A path are around 7 THz, rather close to the maxima along the  $\Gamma$ -K and  $\Gamma$ -M paths (around 5 THz). The upper branches along the  $\Gamma$ -A path are also as flat as the upper branches along the  $\Gamma$ -K and  $\Gamma$ -M paths. In contrast, in the band diagram of the  $\beta$  phase (Fig. 3-b), the acoustic phonon branches highlighted in red along the  $\Gamma$ -A path increase their frequencies almost linearly from the  $\Gamma$ -point to the A-point and reach around 10 THz, along which the group velocity component  $v_{\lambda,z}$  maintains high values. This difference is because the  $\Gamma$ -A path length of the  $\beta$  phase is approximately twice that of  $\alpha$ ; the lattice constant  $c$  of  $\beta$  is nearly half that of  $\alpha$ , owing to the difference in the stacking manner of the basal layers. Normally, optical branches are flat; however, the upper branches along the  $\Gamma$ -A path also have significantly large  $v_{\lambda,z}$ . In Fig. 3-c for the  $\gamma$  phase, the acoustic phonon branches highlighted in red show significant linear dispersions. The frequencies of the longitudinal acoustic modes are 14 and 12.5 THz at the L- and X-points. The frequencies of the transverse acoustic modes are approximately half the values of the longitudinal modes at the L-point and a factor of  $1/\sqrt{2}$  smaller than the longitudinal modes at the X-point, as in the case of fcc rare gas solids<sup>46</sup>. The roughly constant gradients of the branches are large, reflecting the large elastic constants of the  $\gamma$  phase as shown in Table II.

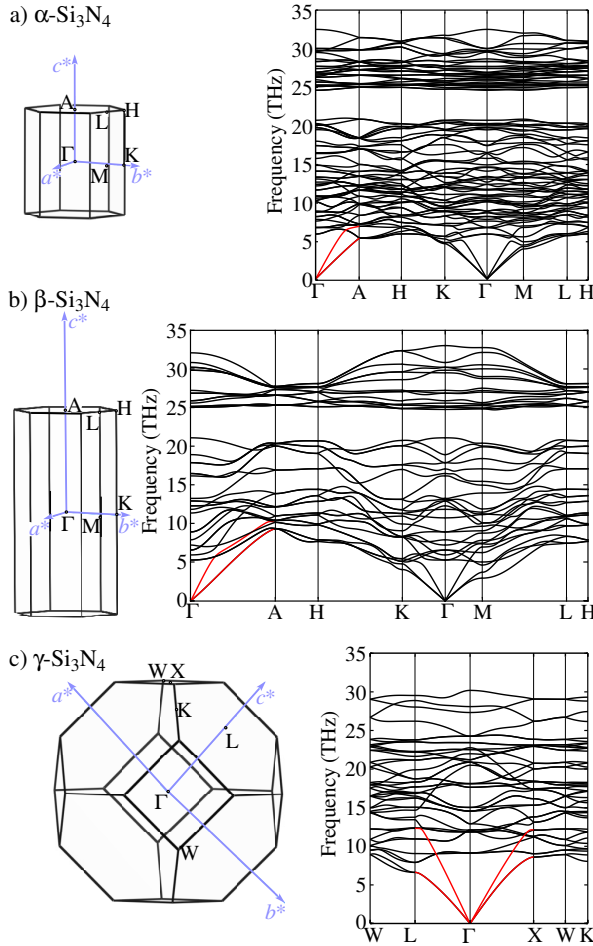


FIG. 3. (color online) Brillouin-zones (left) and calculated phonon band diagrams (right) for three  $\text{Si}_3\text{N}_4$  phases.

### C. $\omega_\lambda$ counter map on reciprocal plane

In another point of view on the group velocities, Fig. 4 shows the cross-sections of the phonon frequency distributions on the  $b^*$ - $c^*$  planes in the first Brillouin-zones. The cross-sections of other planes containing the  $c^*$  axis did not differ much from Fig. 4; thus, we focus on the results for the  $b^*$ - $c^*$  planes as representative of all such planes. We show only the frequencies of four modes from the lowest frequency because they contribute significantly to LTC. Fig. 4-a shows that the frequency distributions and group velocities of  $\alpha\text{-Si}_3\text{N}_4$  are fairly isotropic. On the other hand, in Fig. 4-b of the  $\beta$  phase, the iso-frequency lines in  $0.06 \leq q_{c^*} \leq 0.12 (\text{\AA}^{-1})$  are rather parallel to the  $q_{b^*}$  axis, indicating that the four modes of the  $\beta$  phase, in a significantly large part of the Brillouin zone, have group velocities oriented along the  $c$  axis.

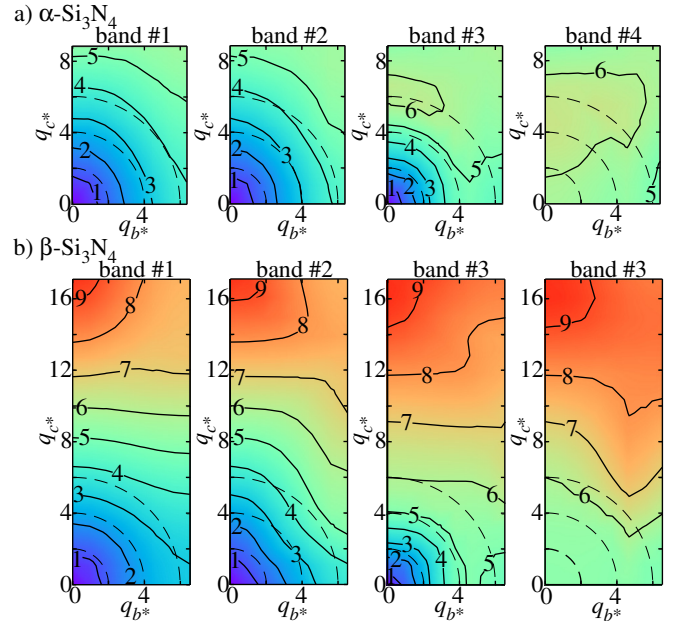


FIG. 4. (color online) Contour maps of phonon frequency (THz) on the  $b^*$ - $c^*$  planes of Brillouin-zones. The maps for the four lowest-frequency phonon states are shown. The frequency landscapes are formed by simply connecting the frequencies of the same band indices, assigned by ascending order of frequency at the respective  $\mathbf{q}$  points.

### D. Frequency-dependences of $\kappa^c$ , $v_\lambda$ and $\Gamma_\lambda$

The microscopic phonon properties we have seen in the previous sections are located in specific paths or planes in the Brillouin zone. In order to more rigorously inspect the LTCs, we examine phonon properties taken over the Brillouin zone. As such properties, in Fig. 5 are shown phonon densities of states (DOS), cumulative thermal conductivities and their frequency derivatives, weighted DOS with the squares of the group velocity components ( $v_{\lambda,x}$  and  $v_{\lambda,z}$ ), and finally, frequency distributions of linewidths.

The first DOS peaks indicated by arrows in Fig. 5-a are related to the flattening of the acoustic branches at the Brillouin zone boundaries. As  $\kappa^c$  increasing up to around 6, 12 and 10 THz for the  $\alpha$ ,  $\beta$  and  $\gamma$  phases in Fig. 5-b, the phonons contributing to the LTCs are mainly located on the frequencies below the first peaks except for the  $\beta$  phase, where almost a half of the contributions to the LTCs are derived from the phonons above the first peak, indicating that the low frequency optical phonons should contribute to these components significantly.

$\kappa^c$  in the  $\gamma$  phase resembles closely to  $\kappa_{xx}^c$  in the  $\beta$  phase, although the linewidths of the  $\gamma$  phase are twice larger than those of the the  $\beta$  phase. Because of the large differences in the crystal structure and the phonon properties in Figs. 5-a,c,d of the  $\gamma$  phase from the  $\alpha$  and  $\beta$  phases, we hereafter focus on the comparison between the latter two phases.

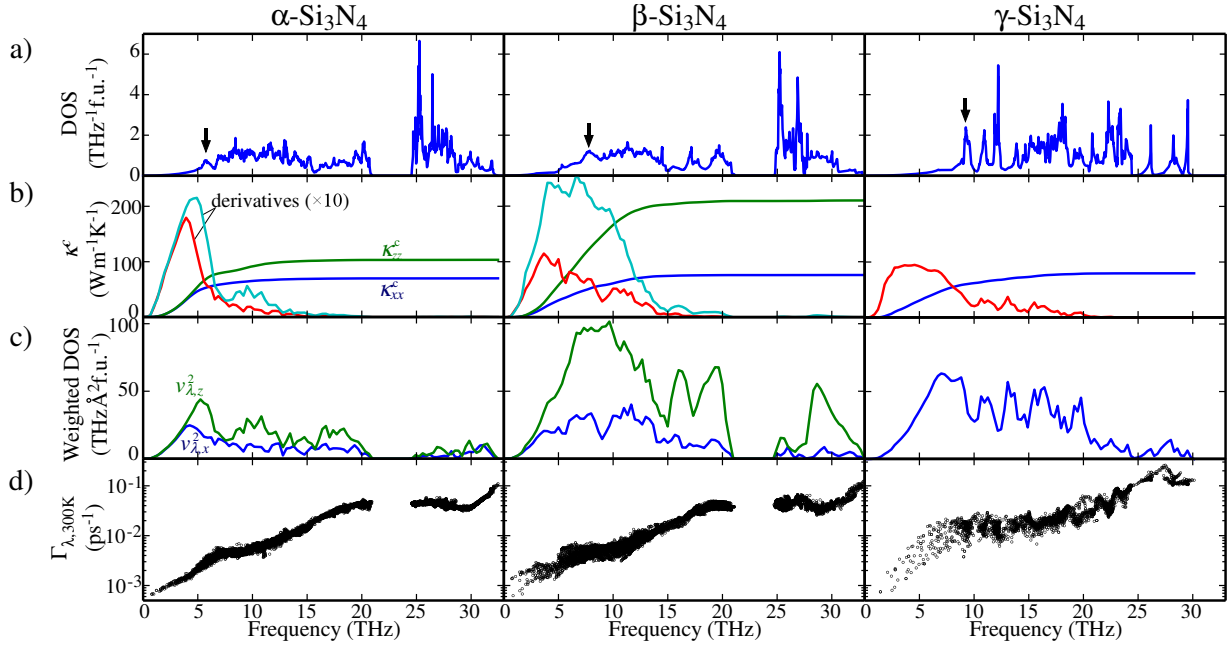


FIG. 5. (color online) Microscopic phonon properties of three  $\text{Si}_3\text{N}_4$  phases. Cumulative thermal conductivity  $\kappa^c$  and its derivative (a), DOS (b), weighted DOS with  $v_{\lambda,i}^2$  (c) and linewidth  $\Gamma_\lambda$  (d).

In Figs. 5-b and c, the directional differences in the derivatives of  $\kappa_{ii}^c$  in the  $\alpha$  and  $\beta$  phases are qualitatively well consistent with the directional differences in the weighted DOS. The relatively larger intensities in the weighted DOS of  $v_{\lambda,z}^2$  in  $\beta\text{-Si}_3\text{N}_4$  critically causes the large anisotropy in its LTCs.

Fig. 5-d shows significantly similar linewidth distributions between the  $\alpha$  and  $\beta$  phases, which let the group velocities alone play the critical role on the different degrees of the anisotropy in the LTCs. Since it is curious that the linewidths are similar between these phases although their group velocities have marked differences, we investigate this similarity further. Previously, Lindsay *et al.* have pointed out a significant positive correlation between LTC and phase space available for the three-phonon scattering according to the selection rules due to the momentum and energy conservation for the three-phonon processes.<sup>47</sup> More recently Togo *et al.* have shown that the frequency profiles of the imaginary part of self-energy  $\Gamma_\lambda(\omega)$ , where  $\Gamma_\lambda(\omega_\lambda) = \Gamma_\lambda$ , are characterized by the three phonon selection rules.<sup>20</sup> In Eq. (1) of the linewidths,  $\Phi_{-\lambda\lambda'\lambda''}$  partly contains the selection rule due to the momentum conservation.<sup>48</sup> In the present study, we examine the impacts on the linewidths of  $\Phi_{-\lambda\lambda'\lambda''}$  and the whole selection rules, one by one.

In Table. III, the magnitudes of  $\Phi_{-\lambda\lambda'\lambda''}$  are compared as the averages over the  $\omega_\lambda$  frequency ranges between 0–15 and 0–35 THz and over all  $\lambda'$  and  $\lambda''$ . The values of the  $\alpha$  and  $\beta$  phases are very close to each other, indicating that  $\Phi_{-\lambda\lambda'\lambda''}$  have similar impacts.

In order to analyze the impacts of the selection rules on the linewidths, we employ the joint density of states

TABLE III. Averages of  $\Phi_{-\lambda\lambda'\lambda''}$  over frequency ranges of  $\omega_\lambda$  (0–15 and 0–35 THz) and all  $(\lambda', \lambda'')$ . The values are in units of  $10^{-10} \text{ eV}^2 \text{f.u.}^{-1}$ .

Frequency Range (THz)	Phase		
	$\alpha$	$\beta$	$\gamma$
0–15	<b>2.66</b>	<b>2.63</b>	5.76
0–30	<b>13.1</b>	<b>13.0</b>	11.4

(JDOS)  $D_2(\mathbf{q}, \omega)$ ,

$$D_2(\mathbf{q}, \omega) = D_2^{(1)}(\mathbf{q}, \omega) + D_2^{(2)}(\mathbf{q}, \omega) \quad (4)$$

where

$$\begin{aligned} D_2^{(1)} &= \frac{1}{N} \sum_{\lambda'\lambda''} \Delta(-\mathbf{q} + \mathbf{q}' + \mathbf{q}'') \\ &\times [\delta(\omega + \omega_{\lambda'} - \omega_{\lambda''}) + \delta(\omega - \omega_{\lambda'} + \omega_{\lambda''})], \\ D_2^{(2)} &= \frac{1}{N} \sum_{\lambda'\lambda''} \Delta(-\mathbf{q} + \mathbf{q}' + \mathbf{q}'') \\ &\times \delta(\omega - \omega_{\lambda'} - \omega_{\lambda''}), \end{aligned}$$

with  $\Delta(\mathbf{x})$  giving 1 if  $\mathbf{x}$  is a reciprocal lattice vector and otherwise zero.

Fig. 6 shows the frequency-dependences of JDOS at different  $\mathbf{q}$ -points on the  $\Gamma\text{-A}$  and  $\Gamma\text{-K}$  paths, which show very slight  $\mathbf{q}$ -point dependence. Eq. (1) includes Bose-Einstein functions for the involved phonon modes and JDOS can be weighted with them as done in refs. 20 and 43, however we omit them for simplicity. With the

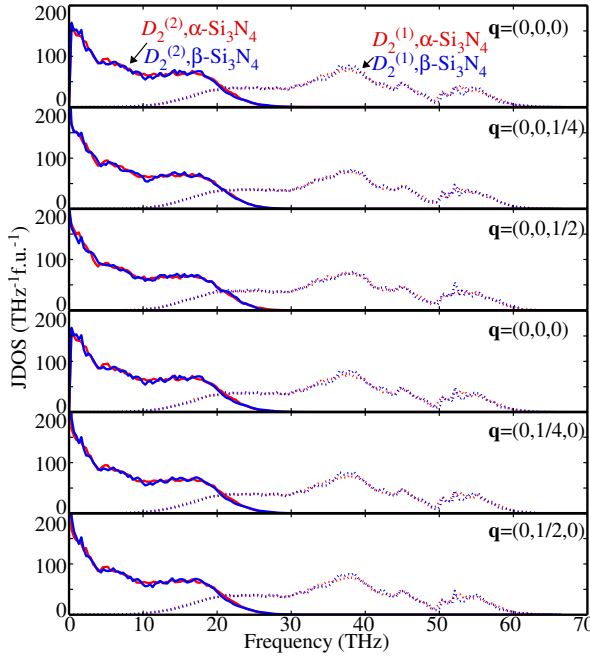


FIG. 6. (color online) JDOS of  $\alpha$ - and  $\gamma$ - $\text{Si}_3\text{N}_4$  at different  $\mathbf{q}$  points. The first and and forth rows are JDOS at the same  $\Gamma$ -point but calculated with the polarization for non-analytic term correction set along  $c^*$  and  $b^*$ , respectively.

weights, the absolute values are affected but the weighted JDOS of the  $\alpha$  and  $\beta$  phases are still similar. At the low frequency region responsible for the LTCs, among the two terms of  $D_2^{(1)}$  and  $D_2^{(2)}$  in Eq. (4), dominant is  $D_2^{(2)}$  which basically corresponds to the half part ( $\omega \geq 0$ ) of the auto-correlation function of DOS, which, for the  $\alpha$  and  $\beta$  phases, commonly show the frequency gap (Fig. 5-a).  $D_2^{(2)}$  curves reflect this DOS feature, dropping suddenly around 0 THz and showing a small shoulder around 5 THz, which corresponds to the width of the gap. Moreover  $D_2^{(2)}$  shows a broad peak around 18 THz, which corresponds to the frequency shift to make the largest correlation between the higher and lower portions of DOS across the gap. Because the gap is basically originated from the differences in the vibrations of the planer  $\text{NSi}_3$  commonly contained in the  $\alpha$  and  $\beta$  phases<sup>45</sup>, the major shapes of  $D_2^{(2)}$ , reflecting this gap feature, are similar in these phases. With the same origin, the JDOS of  $D_2^{(1)}$  are also similar in these phases. With these similar impacts of  $\Phi_{-\lambda\lambda'\lambda''}$  and JDOS on  $\Gamma_\lambda$ ,  $\Gamma_\lambda$  in Fig. 5-d are similar.

As a small but interesting difference in the linewidths between these phases,  $\Gamma_\lambda$  below 5 THz in Fig. 5-d are aligned on a smooth line in the  $\alpha$  phase, while those in the  $\beta$  phase are scattered roughly onto two different lines. This difference can be explained by the vibration directions shown in Fig. 7. In Fig. 7-a,  $\Gamma_\lambda$  are classified using colors according to the sums of the squares of the eigenvector components along  $\mathbf{q}$ ; the sum is 1 for perfectly longitudinal waves. However, these sums have no clear

contrast to distinguish the two branches in the  $\beta$  phase. Fig. 7-b shows the same plot as Fig. 7-a, but with colors according to the sums of the squares of the eigenvector components along the  $a$ - $b$  plane, which has 1 when the eigenvectors lie on the  $a$ - $b$  plane. There is a tendency in the  $\beta$  phase that  $\Gamma_\lambda$  are large for the vibrations along the  $a$ - $b$  plane. Therefore, within the single-mode RTA, for the phonon modes below 5 THz, all of which belong to the acoustic phonon branches, the vibration modes along the  $a$ - $b$  plane are more easily scattered in the  $\beta$  phase, no matter whether they are longitudinal or transverse. For the panel of  $\beta$ - $\text{Si}_3\text{N}_4$  in Fig. 7-b, a straight line can divide the phonon modes into the two groups. The numbers of the phonon modes in the upper and lower parts are 157 and 58, whose ratio is rational as the population ratio of the vibration modes along and out of the  $a$ - $b$  plane.

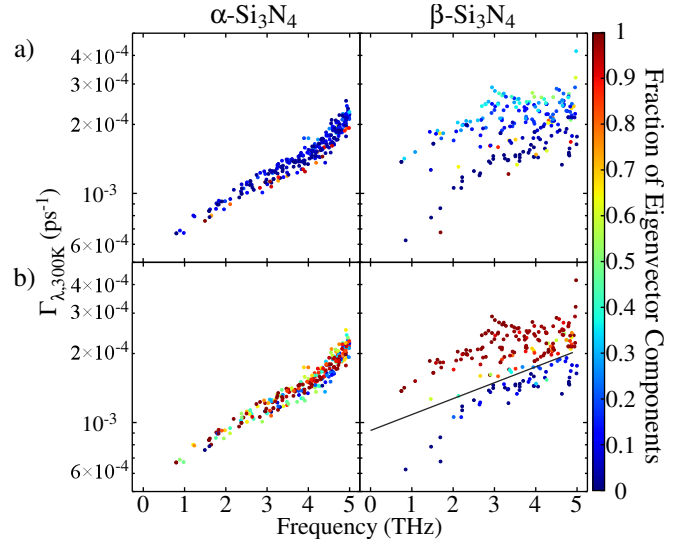


FIG. 7. (color online) Distribution of linewidths  $\omega_\lambda \leq 5$  THz with colormaps with respect to strengths of eigenvector components along  $\mathbf{q}$  (a) and on  $a$ - $b$  plane (b).

#### IV. SUMMARY

In the present study, we investigate the lattice thermal conductivities of the three  $\text{Si}_3\text{N}_4$  phases, by using the lattice dynamics based on the *ab-initio* interatomic force constants. The main remarks are as follows:

- 1) In the  $\alpha$ - and  $\beta$ - $\text{Si}_3\text{N}_4$ , whose crystal structures are characterized by the stacking manners of the basal layers, which alter the LTCs. In  $\alpha$ - $\text{Si}_3\text{N}_4$ , the LTC tensors are rather isotropic, while  $\kappa_{zz}$  of the  $\beta$  phase is much larger than the others, showing remarkable anisotropy in the LTC tensor.
- 2) In the  $\alpha$  phase, the acoustic mode phonons below 6 THz are the main heat carriers, while in the  $\beta$  phase, the phonons below 12 THz contribute to the thermal conductivity. Their group velocities are significantly different between the phases; their linewidths are basically similar

due to the similar impacts of the phonon-phonon interaction strengths and selection rules. Therefore the difference in the group velocities alone qualitatively explains the difference of anisotropy.

3) In the  $\gamma$  phase, the frequency distribution of the phonon mode contributions to LTC is found to be similar to that for  $\kappa_{xx}$  of  $\beta\text{-Si}_3\text{N}_4$  although the respective phonon properties (group velocities and linewidths) are much different from those of the other phases

## ACKNOWLEDGMENTS

The present work was partly supported by Grants-in-Aid for Scientific Research of MEXT, Japan (Grant No. 15K14108 and ESISM (Elements Strategy Initiative for Structural Materials) of Kyoto University).

## Appendix A: Pressure dependence of LTC of $\gamma$ -phase

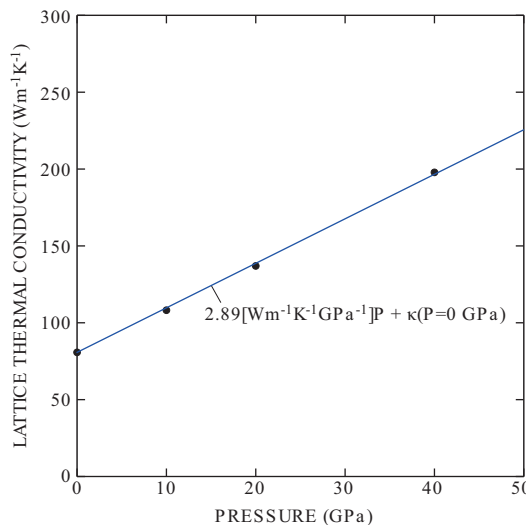


FIG. 8. (color online) Pressure dependence of LTC of  $\gamma\text{-Si}_3\text{N}_4$ .

\* k-tatsumi@imass.nagoya-u.ac.jp

<sup>1</sup> G. Slack, Journal of Physics and Chemistry of Solids **34**, 321 (1973).

<sup>2</sup> Y. Zhou, H. Hyuga, D. Kusano, Y.-i. Yoshizawa, and K. Hirao, Advanced Materials **23**, 4563 (2011).

<sup>3</sup> K. Hirao, K. Watari, H. Hayashi, and M. Kitayama, MRS Bulletin **26**, 451 (2001).

<sup>4</sup> K. Watari, Journal of the Ceramic Society of Japan **109**, S7 (2001).

<sup>5</sup> N. Hirosaki, Y. Okamoto, M. Ando, F. Munakata, and Y. Akimune, Journal of the Ceramic Society of Japan **104**,

49 (1996).

<sup>6</sup> F. L. Riley, Journal of the American Ceramic Society **83**, 245 (2000).

<sup>7</sup> M. Yashima, Y. Ando, and Y. Tabira, The Journal of Physical Chemistry B **111**, 3609 (2007).

<sup>8</sup> D. Du Boulay, N. Ishizawa, T. Atake, V. Streltsov, K. Furuya, and F. Munakata, Acta Crystallographica Section B: Structural Science **60**, 388 (2004).

<sup>9</sup> S. Hampshire, H. Park, D. Thompson, and K. Jack, Nature **274**, 880 (1978).

- <sup>10</sup> T. Hahn, ed., International tables for crystallography, Vol. A (John Wiley & Sons, Inc., 2011).
- <sup>11</sup> B. Li, L. Pottier, J. Roger, D. Fournier, K. Watari, and K. Hirao, *Journal of the european ceramic society* **19**, 1631 (1999).
- <sup>12</sup> T. Takahashi, M. Sado, N. Sugimoto, J. Tatami, M. Iijima, S. Inagaki, Y. Kubota, I. Yamamoto, and S. Tanaka, *Advanced Powder Technology* **27**, 2005 (2016).
- <sup>13</sup> K. Hirao, K. Watari, M. Brito, M. Toriyama, and S. Kanazaki, *Journal of the American Ceramic Society* **79**, 2485 (1996).
- <sup>14</sup> X.-W. Zhu, Y. Sakka, Y. Zhou, K. Hirao, and K. Itatani, *Journal of the European Ceramic Society* **34**, 2585 (2014).
- <sup>15</sup> Y. Akimune, F. Munakata, K. Matsuo, N. Hirosaki, Y. Okamoto, and K. Misono, *J Ceram Soc Jpn*, 107 (1999), pp. 339-3427 **107**, 339 (1999).
- <sup>16</sup> Y. Yamamoto, N. Hirosaki, I. Ishikawa, J. YE, K. Matsuo, K. Furuya, F. Munakata, and Y. Akimune, *Journal of the Ceramic Society of Japan* **108**, 515 (2000).
- <sup>17</sup> K. Watari, L. Pottier, B. Li, D. Fournier, and M. Toriyama, *Ceramic Transactions(USA)* **118**, 341 (2000).
- <sup>18</sup> N. Hirosaki, S. Ogata, C. Kocer, H. Kitagawa, and Y. Nakamura, *Physical Review B* **65**, 134110 (2002).
- <sup>19</sup> R. Vashishta, R. K. Kalia, A. Nakano, and I. Ebbssö, Amorphous Insulators and Semiconductor, edited by M. F. Thorpe and M. I. Mitkova (Kluwer, 1996).
- <sup>20</sup> A. Togo, L. Chaput, and I. Tanaka, *Physical Review B* **91**, 094306 (2015).
- <sup>21</sup> A. Zerr, G. Miehe, G. Serghiou, M. Schwarz, E. Kroke, R. Riedel, H. Fueß, P. Kroll, and R. Boehler, *Nature* **400**, 340 (1999).
- <sup>22</sup> Y. Zhang, A. Navrotsky, and T. Sekine, *Journal of materials research* **21**, 41 (2006).
- <sup>23</sup> B. Xu, J. Dong, P. F. McMillan, O. Shebanova, and A. Salamat, *Physical Review B* **84**, 014113 (2011).
- <sup>24</sup> D. Morelli and J. Heremans, *Applied physics letters* **81**, 5126 (2002).
- <sup>25</sup> L. Chaput, *Physical review letters* **110**, 265506 (2013).
- <sup>26</sup> S.-i. Tamura, *Physical Review B* **27**, 858 (1983).
- <sup>27</sup> A. Togo and I. Tanaka, *Scripta Materialia* **108**, 1 (2015).
- <sup>28</sup> P. E. Blöchl, *Phys. Rev. B* **50**, 17953 (1994).
- <sup>29</sup> G. Kresse and J. Furthmüller, *Physical review B* **54**, 11169 (1996).
- <sup>30</sup> G. Kresse, *J. Non-Cryst. Solids* **193**, 222 (1995).
- <sup>31</sup> D. J. Kresse, Georg, *Phys. Rev. B* **59**, 1758 (1999).
- <sup>32</sup> J. P. Perdew, K. Burke, and M. Ernzerhof, *Phys. Rev. Lett.* **77**, 3865 (1996).
- <sup>33</sup> W. Paszkowicz, R. Minikayev, P. Piszora, M. Knapp, C. Bähtz, J. Recio, M. Marques, P. Mori-Sánchez, L. Gerward, and J. Jiang, *Phys. Rev. B* **69**, 052103 (2004).
- <sup>34</sup> D. M. Ceperley and B. Alder, *Physical Review Letters* **45**, 566 (1980).
- <sup>35</sup> S. Wei and M. Chou, *Physical review letters* **69**, 2799 (1992).
- <sup>36</sup> Y. Wang, J. Wang, W. Wang, Z. Mei, S. Shang, L. Chen, and Z. Liu, *J. Phys.: Condens. Matter* **22**, 202201 (2010).
- <sup>37</sup> M. T. Dove, Introduction to lattice dynamics, Vol. 4 (Cambridge university press, 1993) pp. 76–77.
- <sup>38</sup> A. Ward and D. Broido, *Physical Review B* **81**, 085205 (2010).
- <sup>39</sup> R. Minikayev, W. Paszkowicz, P. Piszora, M. Knapp, and C. Bähtz, “Thermal expansion of and silicon nitride,” (2007).
- <sup>40</sup> P. Andersson, *Journal of Physics C: Solid State Physics* **18**, 3943 (1985).
- <sup>41</sup> A. Cepellotti and N. Marzari, *Physical Review X* **6**, 041013 (2016).
- <sup>42</sup> R. J. Hardy, *Physical Review B* **2**, 1193 (1970).
- <sup>43</sup> S. Mukhopadhyay, L. Lindsay, and D. J. Singh, *Scientific reports* **6** (2016).
- <sup>44</sup> T. Hirai, S. Hayashi, and K. Niihara, AM. CERAM. SOC. BULL. Am. Ceram. Soc. Bull. **57**, 1126 (1978).
- <sup>45</sup> A. Kuwabara, K. Matsunaga, and I. Tanaka, *Physical Review B* **78**, 064104 (2008).
- <sup>46</sup> M. T. Dove, Introduction to lattice dynamics, Vol. 4 (Cambridge university press, 1993) pp. 30–31.
- <sup>47</sup> L. Lindsay and D. A. Broido, *J. Phys.: Condens. Matter* **20**, 165209 (2008).
- <sup>48</sup> D. C. Wallace, Thermodynamics of Crystals (John Wiley & Sons, Inc., 1972) Chap. 10.